# A coupled DAS shaped-fibre and 3D elastic finite difference wave model

Matt Eaid, Junxiao Li and Kris Innanen

## ABSTRACT

The interest in Distributed Acoustic Sensing (DAS) fibres, for improved geophysical acquisition, has seen substantial growth over the last half decade. The ability to drive down acquisition costs, improve repeatability, and expand the application of seismic acquisition are all attractive properties of DAS technologies. While applications of straight DAS fibres have proven successful, their well known broadside insensitivity greatly limits their application. Research efforts have recently shifted to creating fibres in more complicated shapes, such as helices, to better characterize, and recover the wavefield. These technologies show promise in negating the effects of broadside insensitivity, however, the interpretation of seismic signals recorded on helically-wound fibres is not well understood. In order to learn more about how the signal captured by shaped fibres relates to the signal captured by conventional geophones, it is imperative to develop full 3D elastic modeling tools to investigate the response of fibres of arbitrary shape, in the presence of elastic wavefields. We begin with a discussion of the geometrical model of fibres of arbitrary shape, and how they measure the seismic wavefield. We then discuss the velocity-stress method of 3D elastic wave propagation, and how it may be extended to apply to DAS fibres. Finally, we conclude with some examples of elastic wave modeling using DAS fibres, and discuss how this technology will expand.

## INTRODUCTION

For decades the standard geophone has been the instrument of choice in the measurement of seismic wavefields. The current economic environment, coupled with a change in the role of seismic acquisition has driven the need for innovative seismic acquisition technologies. One such technology, referred to as Distributed Acoustic Sensing (DAS) has gained substantial popularity, and in recent years has seen a drastic increase in the literature. DAS utilizes standard telecommunication optical fibres, instead of conventional geophones, to sense seismic motion. The recent explosion in fibre-optics for telecommunication has greatly reduced the cost of optical fibres, and has made them an attractive option in the acquisition of seismic wavefields.

Recent publications have explored diverse applications of Distributed Acoustic Sensing. Daley et al. (2013), Mateeva et al. (2014), and Mestayer et al. (2012) examine the use of straight DAS fibres for vertical seismic profiles. Application of DAS to VSP has the attractive advantages of being less intrusive then geophones, reducing cost of acquiring data by eliminating the need for well shut down, and protecting the borehole from damage. Additionally, DAS fibres may be permanently installed in the casing over the full length of the well, reducing costs of repeat surveys, and improving seismic coverage around the well. Martin et al. (2017) examined using an array of DAS fibres for the passive monitoring of teleseismic waves, and anthropogenic noise. While Webster et al. (2016) employed straight fibres in deviated wells to detect microseismic events during fracking. They found that the

DAS system detected fewer events than standard geophones, but with increased accuracy due to a denser array of channels.

Much of the early research on Distributed Acoustic Sensing focused on the application of the common, straight, telecommunication fibres. However, due to the rigid nature of the materials that optical fibres are constructed from, they are only sensitive to seismic strain parallel to the fibre. In other words, DAS fibres are only sensitive to seismic strain directed along the tangent of the fibre. Straight fibres only sample a single tangent direction, having a strong negative impact on the recorded signal in walk-away VSP and near-offset surface seismic applications. Kuvshinov (2015) discusses the theoretical aspects and the effect the angle of incidence has on the recorded signal.

A natural remedy to this problem, is simply to increase the number of unique tangent directions that a fibre samples. Fortunately, this can be achieved by simply altering the geometry of the fibre, in a manner that samples a large number of unique tangents over a small spatial extent. Kuvshinov (2015) and Hornman (2017), explore the use of a fibre wound around the cable in a helix. Kuvshinov (2015) showed that helically wound fibres were more robust to perpendicular wavefields, while Hornman (2017) showed much better correlation between hydrophone data and hellically wound fibre data, then between hydrophones and straight fibres for surface seismic. While tests on helically wound fibres have been encouraging, they still only capture a small number of tangents. For full-scale strain tensor recovery we need to sample as many tangents as possible. Innanen (2017) discussed the idea of nested N-helices, and showed that as the degree of nesting increases, the number of tangents sampled rapidly increases.

Unfortunately, as the number of tangents increases the complexity of the recorded signal grows. So much so that it can be hard to interpret, and discern exactly what the signal represents. For Distributed Acoustic Sensing to takeoff we must be able to sample as many tangents as possible, and be able to discern what the corresponding signal means. We develop an elastic wave model, coupled with the complex geometric model proposed by Innanen (2017), in order to be able to accurately model the response of an arbitrarily shaped DAS fibre in the presence of elastic waves.

## Physics of Distributed Acoustic Sensing

The interaction of light with matter, is in general a very complicated process. Light interacting with small particles has a tendency to scatter, and often a scale factor has to be introduced to predict the type of scattering.

$$x = \frac{2\pi r}{\lambda} \tag{1}$$

In the case when, $x \ll 1$, light scatters according to what is known as Rayleigh scattering. Rayleigh scattering, arises from the ability of molecules to become polarized. As the oscillating electric field of the light wave encounters a particle, it acts on the electric charges, causing the particle to oscillate at the same frequency. The oscillating particle then acts as a radiating dipole, radiating backscattered light. Optical fibres contain microscopic impurities acting as centers for Rayleigh scattering. As a laser pulse traverses the fibre, some of

the light is backscattered and recorded by what is known as the interrogator unit. When a fibre is strained by seismic energy, it is stretched and squeezed along the fibre tangent, and the distance between the scattering impurities changes, altering the pattern of backscattered light. The alteration of the backscattered light is interpreted by the interrogator as seismic strain.

## GEOMETRICAL MODEL OF DAS FIBRES.

The interrogator is able to discern where along the arc length of the fibre a signal has come from, but how this translates to Cartesian coordinates in the seismic experiment is of more importance, and requires careful consideration of the geometry of the DAS fibre-cable system. Additionally, the construction of a three dimensional elastic wave modeling tool, requires precise information about the cable, and fibre positions to project the signal onto. Some results from differential geometry are required for this discussion, in which I used the text Pressley (2010), additionally much of this discussion follows from Innanen (2017). To accurately model the elastic wavefield, we must carefully keep track of both the cable and fibre geometry, by keeping track of

1. Cable geometry
   (a) Cable axis (in Cartesian or parametric coordinates)
   (b) Arc length along cable axis
   (c) Tangents of cable axis
2. Fibre geometry
   (a) Fibre axis (in Cartesian or parametric coordinates)
   (b) Fibre arc length
   (c) Tangents of fibre

We will begin with a discussion of the cable, and then will tackle the idea of the fibre geometry.

### Cable geometry

*(a) Axial geometry*

Consider an arbitrarily shaped cable in a Cartesian coordinate system figure 1 (a). The arc length ($s'$) is then the distance, along the cable, from the start of the cable to any point along it. Let **c** be a vector pointing from the origin to the point at the distance $s'$, as shown in figure 1 (c).

$$\mathbf{c}(s') = \begin{bmatrix} c_1(s') \\ c_2(s') \\ c_3(s') \end{bmatrix} \tag{2}$$

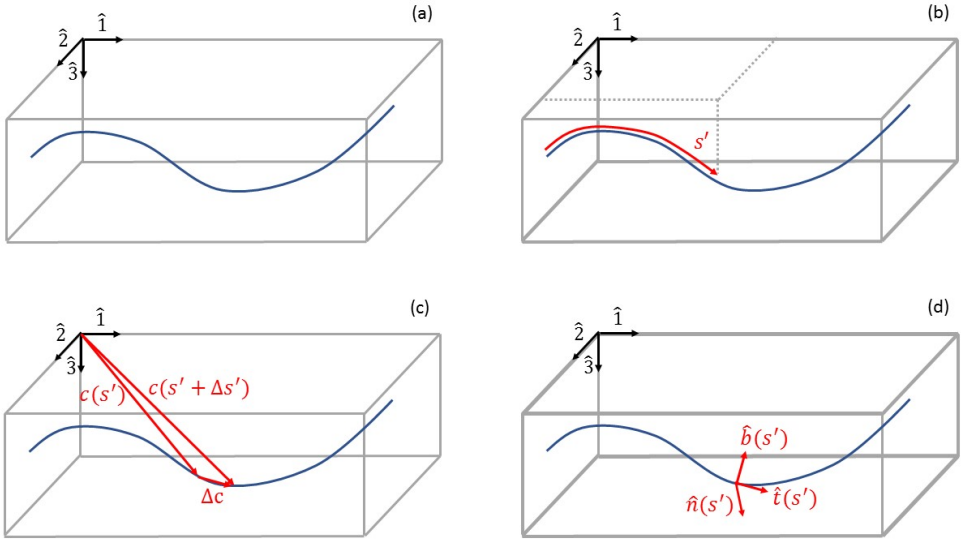


FIG. 1. (a) Arbitrary cable **c** in a 3D Cartesian grid, (b) Arc length along the curve described as distance from starting point of curve to a point along the curve, (c) Knowing the arc length we can calculate position of the vector parameterized by arc length, (d) Calculating the position at two nearby points and taking the difference allows for calculation of the tangent directions, we then may label the curve by a new system in $\hat{t}(s')$, $\hat{n}(s')$, and $\hat{b}(s')$.

The vector **c**(s') of equation (2) then describes the cable axis in the Cartesian system described by the unit vectors $\{\hat{\mathbf{x}}_1, \hat{\mathbf{x}}_2, \hat{\mathbf{x}}_3\}$. It turns out to be more practical to parameterize **c** by one of the Cartesian coordinates instead of the arc length, letting $c_1 = x$, the new vector becomes,

$$\mathbf{c}(x) = \begin{bmatrix} x \\ c_2(x) \\ c_3(x) \end{bmatrix} \tag{3}$$

*(b) Cable arc length*

The length of any vector, **v** in space $\mathbb{R}^n$ is equal to the the $L_2$ norm of that vector,

$$||\mathbf{v}|| = \mathbf{v} \cdot \mathbf{v} = \sqrt{v_1^2 + ... + v_n^2} \tag{4}$$

Given any two points on a curve **c** the vector connecting them is $\mathbf{c}(x' + \Delta x') - \mathbf{c}(x')$. As $\Delta x \to 0$, the direction of $\mathbf{c}(x' + \Delta x') - \mathbf{c}(x')$ approaches that of the derivative, defined by

$$\frac{d\mathbf{c}}{dx'} = \lim_{\Delta x \to 0} \frac{c(x' + \Delta x') - c(x')}{\Delta x} \tag{5}$$

As $\Delta x \to 0$, the derivative approximates the curve. Summation of the small derivative lengths gives the total arc length along the curve.

$$s'(x) = \int_0^x dx' \left[ \frac{d\mathbf{c}}{dx'} \cdot \frac{d\mathbf{c}}{dx'} \right]^{1/2} = \int_0^x dx' \left[ 1 + \left( \frac{dc_2}{dx'} \right)^2 + \left( \frac{dc_3}{dx'} \right)^2 \right]^{1/2} \tag{6}$$

*(c) Cable tangents*

Optical fibers are only sensitive to seismic strain components directed along their axis, described by the tangent directions, due to the rigid nature of optical glass. Thus, while it is important to keep track of the cable axis in Cartesian coordinates, it is even more important to keep track of the tangent directions at all points. We must then develop a new set of orthogonal directions that vary along the curve, such that one of the orthogonal vectors is always directed along the cable tangent. Naturally, because this coordinate system varies along the cable axis, each orthogonal vector will be a function of the arc length ($s'$).

Consider the two closely spaced points of figure 1 (c), separated by distance $||\Delta\mathbf{c}||$. The direction of $\Delta\mathbf{c}$ approaches the tangent of the cable in the limit that the distance between these two points goes to zero, given by the vector difference between $\mathbf{c}(s'+\Delta s')$ and $\mathbf{c}(s')$. Normalizing by the distance gives the unit vector, therefore the unit tangent has definition,

$$\hat{\mathbf{t}}(s') = \frac{d\mathbf{c}}{ds'} = \lim_{\Delta s' \to 0} \frac{\mathbf{c}(s'+\Delta s') - \mathbf{c}(s')}{\Delta s'} \tag{7}$$

As the tangent varies along the curve we may describe two additional vectors which lie in a plane perpendicular to the tangent. Since the tangent vector of equation (7) has length 1,

$$\hat{\mathbf{t}}(s') \cdot \hat{\mathbf{t}}(s') = 1$$
$$\frac{d\hat{\mathbf{t}}(s')}{ds'} \cdot \hat{\mathbf{t}} + \hat{\mathbf{t}} \cdot \frac{d\hat{\mathbf{t}}(s')}{ds'} = 0$$
$$\frac{d\hat{\mathbf{t}}(s')}{ds'} \cdot \hat{\mathbf{t}} = 0$$

the derivative of $\hat{\mathbf{t}}(s')$, $\left(\frac{d\hat{\mathbf{t}}(s')}{ds'}\right)$, is perpendicular to $\hat{\mathbf{t}}(s')$, and is referred to as the normal.

$$\hat{\mathbf{n}}(s') = \frac{d\hat{\mathbf{t}}(s')}{ds'} \tag{8}$$

A third vector may defined through the simple cross product of the the normal and tangent vector, which is commonly referred to as the binormal,

$$\hat{\mathbf{b}}(s') = \hat{\mathbf{t}}(s') \times \hat{\mathbf{n}}(s') \tag{9}$$

We now have a coordinate system that varies along the cable axis described by the three orthogonal vectors $\{\hat{\mathbf{t}}(s'), \hat{\mathbf{n}}(s'), \hat{\mathbf{b}}(s')\}$, as illustrated in figure 1 (d).

## Fibre Geometry

In the limiting case of a straight fibre, the cable, which may be of arbitrary shape, and the fibre, share the same geometric properties due to the fact the fibre is embedded in the cable, and the thickness of the cable makes them coaxial. It is more desirable to have a fibre that may be of arbitrary wind, increasing the complexity of the geometric problem, but also increasing the number of sampled tangents, and therefore increasing the sampling of the whole wavefield (Innanen, 2017). In the general case we must define the fibre position, as well as the arc length, and tangents of the fibre.

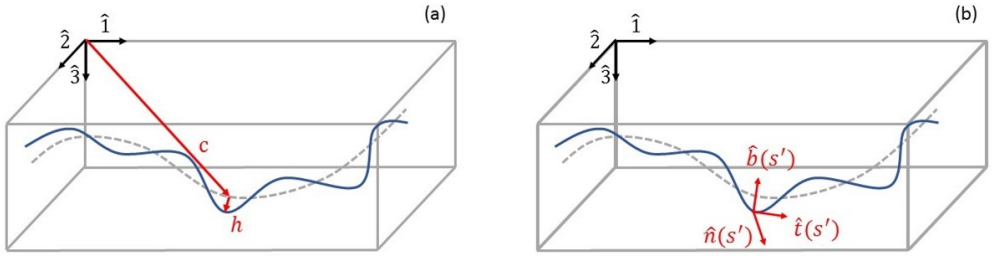


FIG. 2. (a) The vector representation of the fibre **f** may be represented as the summation of a vector pointing from the origin to the cable **c**, and a vector pointing from the point on the cable to the fibre **h**, (b) the tangent, normal, and binormal for the fibre.

*(a) Fibre position.*

Although a fibre may theoretically take the shape of any general curve, their are practical and physical constraints of the fibre that make well defined geometric winds more desirable. One such wind is the helix and nested helices described by Innanen (2017). For simplicity we will look only at these two cases, however, this discussion holds in the general case. In general, the position of the fibre, as shown in figure 2 may be written as,

$$\mathbf{f} = \mathbf{c} + \mathbf{h} = \begin{bmatrix} c_1(s') \\ c_2(s') \\ c_3(s') \end{bmatrix} + \begin{bmatrix} h_1(s') \\ h_2(s') \\ h_3(s') \end{bmatrix} \tag{10}$$

The vector **h** in equation (10) is simply a vector pointing from the cable axis to the fibre, and as such exists in the frame $\{\hat{\mathbf{t}}(s'), \hat{\mathbf{n}}(s'), \hat{\mathbf{b}}(s')\}$. A helix at a given point takes the parametric form of a circle around the central axis of the cable, and as such **h**, in the $\{\hat{t}, \hat{n}, \hat{b}\}$ frame, has the parametric form (Innanen, 2017),

$$\mathbf{h} = \begin{bmatrix} 0 \\ r\cos(s'/v) \\ r\sin(s'/v) \end{bmatrix} \tag{11}$$

This parameterization leads to,

$$\mathbf{f} = \mathbf{c} + \mathbf{h} = \begin{bmatrix} c_1(s') \\ c_2(s') \\ c_3(s') \end{bmatrix} + \begin{bmatrix} \hat{\mathbf{1}}\cdot\hat{\mathbf{t}}(s') & \hat{\mathbf{1}}\cdot\hat{\mathbf{n}}(s') & \hat{\mathbf{1}}\cdot\hat{\mathbf{b}}(s') \\ \hat{\mathbf{2}}\cdot\hat{\mathbf{t}}(s') & \hat{\mathbf{2}}\cdot\hat{\mathbf{n}}(s') & \hat{\mathbf{2}}\cdot\hat{\mathbf{b}}(s') \\ \hat{\mathbf{3}}\cdot\hat{\mathbf{t}}(s') & \hat{\mathbf{3}}\cdot\hat{\mathbf{n}}(s') & \hat{\mathbf{3}}\cdot\hat{\mathbf{b}}(s') \end{bmatrix} \begin{bmatrix} 0 \\ r\cos(s'/v) \\ r\sin(s'/v) \end{bmatrix} \tag{12}$$

where the first term on right hand side of the addition is a rotation matrix that rotates **h** from $\{\hat{\mathbf{t}}(s'), \hat{\mathbf{n}}(s'), \hat{\mathbf{b}}(s')\}$ to $\{\hat{\mathbf{1}}, \hat{\mathbf{2}}, \hat{\mathbf{3}}\}$. Equation (12) gives the position of the helically wound fibre about an arbitrary cable, in Cartesian coordinates.

*(b) Fibre arc length*

It is important to keep track of the fibre arc length, when the interrogator detects seismic strain, it places the the strain at a distance $s$ along the fibre. Keeping careful track of the

fibre arc length allows us to know where in space a particular measurement has come from. Using the definition of arc length from equation (6), the arc length along the fibre is,

$$s = \left[1 + \frac{r^2}{v^2}\right]^{1/2} s' \tag{13}$$

*(c) Fibre tangents*

We may re-parameterize the fibre position in terms of total arc length $s$ by making the change of variables,

$$s'(s) = \left[1 + \frac{r^2}{v^2}\right]^{-1/2} s \tag{14}$$

Additionally if we let $f_1 = x$, $f_2 = f_2(x)$, $f_3 = f_3(x)$, and $s = s(x)$ then

$$s(x) = \int_0^x dx' \left[1 + \left(\frac{df_2}{dx'}\right) + \left(\frac{df_3}{dx'}\right)\right]^{1/2} \tag{15}$$

and finally,

$$\hat{\mathbf{t}}(s) = \frac{d\mathbf{f}}{ds} \tag{16}$$

The fibre tangent contained in equation (16) is arguably the most important quantity in geometric models for Distributed Acoustic Sensing systems, and finite difference modeling. The projection of seismic strain onto this tangent direction produces the signal in DAS systems, and our model.

## ELASTIC WAVE MODEL FOR DAS

Distributed Acoustic Sensing fibres are sensitive to seismic strain in the direction explored by the tangent of the fibre. As such we must develop an elastic wave model which provides us with information about the full strain tensor. The strain tensor must then be rotated onto the fibre tangent to model the signal a real fibre would capture.

### Velocity-Stress finite difference

Velocity-stress finite difference relies on measurements of the particle velocity and stress to propagate the wavefield, and relies on three key formulas from theoretical seismology (Yomogida and Etgen, 1993),

1. Elastodynamic equation of motion

$$\rho \frac{\partial^2 u_i}{\partial t^2} = \nabla \cdot \sigma + f_i = \sum_{j=1}^{3} \frac{\partial \sigma_{ij}}{\partial x_j} + f_i \tag{17}$$

2. Hooke's Law (stress-strain relation)

$$\sigma_{ij} = C_{ijkl} e_{kl} \tag{18}$$

3. Strain Tensor

$$e_{kl} = \frac{1}{2}\left(\frac{\partial u_k}{\partial x_l} + \frac{\partial u_l}{\partial x_k}\right) \tag{19}$$

**Velocity-Stress method in one dimension.**

Consider a vertical medium with a p-wave propagating in the $z$ direction. In this case only the components, $u_z$ and $\sigma_{zz}$ are nonzero, and as with most exploration seismic applications the body force $f_i$ may be neglected. In this case the equation of motion (17) and Hooke's Law (18) reduce to,

$$\rho \frac{\partial^2 u_z}{\partial t^2} = \frac{\partial \sigma_{zz}}{\partial z} \tag{20}$$

and,

$$\sigma_{zz} = (\lambda + 2\mu) e_{zz} \tag{21}$$

Now taking the time derivative of equation (21), with the definition of the strain tensor from equation (19), we have the set of coupled first order differentials,

$$\rho \frac{\partial \dot{u}_z}{\partial t} = \frac{\partial \sigma_{zz}}{\partial z} \tag{22}$$

$$\frac{\partial \sigma_{zz}}{\partial t} = (\lambda + 2\mu) \frac{\partial \dot{u}_z}{\partial z} \tag{23}$$

where $\dot{u} = \frac{\partial u}{\partial t}$ is the particle velocity.

Equations (22) and (23) represent a coupled system of partial differential equations in particle velocity $\dot{u}$ and stress $\sigma$, that when solved propagate a wavefield. The system of equations could be solved on one grid by central finite difference approximations (CFDA). However, a more stable scheme involves solving equation (22) on one grid using CFDA, and solving equation (23) on a grid staggered by half a step in time and depth with forward finite differences (FFDA), shown in figure 3 (Krebes, 2010).

$$\frac{\dot{u}_k^{n+1/2} - \dot{u}_k^{n-1/2}}{\tau} = \frac{1}{\rho_k} \frac{\sigma_{k+1/2}^n - \sigma_{k-1/2}^n}{\Delta z} \tag{24}$$

$$\frac{\sigma_{k+1/2}^{n+1} - \sigma_{k+1/2}^n}{\tau} = (\lambda + 2\mu)_{k+1/2} \frac{\dot{u}_{k+1}^{n+1/2} - \dot{u}_k^{n+1/2}}{\Delta z} \tag{25}$$

Equations (24), and (25) are the finite difference representations of equations (22), and (23) on a staggered grid. Referencing figure 3, the computation proceeds in the following manner. Assuming that we know the value of the velocity and stress at every depth, up to and including time $n$, then we may compute $\dot{u}$ at time step $n + 1/2$. For instance, the velocity $\dot{u}$ at point $P$ is calculated using the stresses at $A$ and $C$ and the velocity at $B$. Similarly, the velocity at point $Q$ is computed from stresses at $C$ and $F$ and the velocity at $D$. Once the velocity at every depth for time $n + 1/2$ is calculated, stresses at time $n + 1$ are calculated in a similar fashion. The computations then proceed in a leapfrog pattern, until velocity and stress are computed at every depth for all time levels.

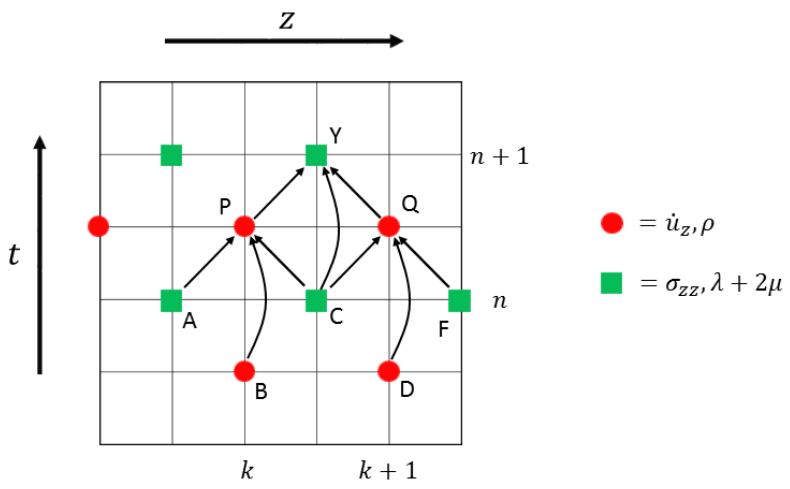


FIG. 3. Staggered grid required for solution of the 1D velocity-stress finite difference equations.

**Velocity-Stress method in two dimensions.**

We now consider a medium in $x - z$, where the additional components $\sigma_{xx}$, $\sigma_{xz}$, and $u_x$ are now nonzero. Our problem now becomes solving the set of equations,

$$\frac{\partial \dot{u}_x}{\partial t} = \frac{1}{\rho}\left(\frac{\partial \sigma_{xx}}{\partial x} + \frac{\partial \sigma_{xz}}{\partial z}\right) \tag{26}$$

$$\frac{\partial \dot{u}_z}{\partial t} = \frac{1}{\rho}\left(\frac{\partial \sigma_{zz}}{\partial z} + \frac{\partial \sigma_{xz}}{\partial x}\right) \tag{27}$$

$$\frac{\partial \sigma_{xx}}{\partial t} = (\lambda + 2\mu)\frac{\partial \dot{u}_x}{\partial x} + \lambda \frac{\partial \dot{u}_z}{\partial z} \tag{28}$$

$$\frac{\partial \sigma_{zz}}{\partial t} = (\lambda + 2\mu)\frac{\partial \dot{u}_z}{\partial z} + \lambda \frac{\partial \dot{u}_x}{\partial x} \tag{29}$$

$$\frac{\partial \sigma_{xz}}{\partial t} = \mu\left(\frac{\partial \dot{u}_x}{\partial z} + \frac{\partial \dot{u}_z}{\partial x}\right) \tag{30}$$

where the stiffness matrix $C_{ijkl}$ used is the typical one for an isotropic medium.

$$C = \begin{bmatrix} \lambda + 2\mu & \lambda & \lambda & 0 & 0 & 0 \\ \lambda & \lambda + 2\mu & \lambda & 0 & 0 & 0 \\ \lambda & \lambda & \lambda + 2\mu & 0 & 0 & 0 \\ 0 & 0 & 0 & \mu & 0 & 0 \\ 0 & 0 & 0 & 0 & \mu & 0 \\ 0 & 0 & 0 & 0 & 0 & \mu \end{bmatrix} \tag{31}$$

Equations (26)-(30) are now solved on grids that are staggered in time, and space as shown in figure 4. The solution to the 2D velocity-stress finite difference is similar in nature to the 1D case, and a full discussion will not be included, as the 3D method will be discussed in detail, interested readers may turn their attention to Virieux (1986) for full details of the 2D method.

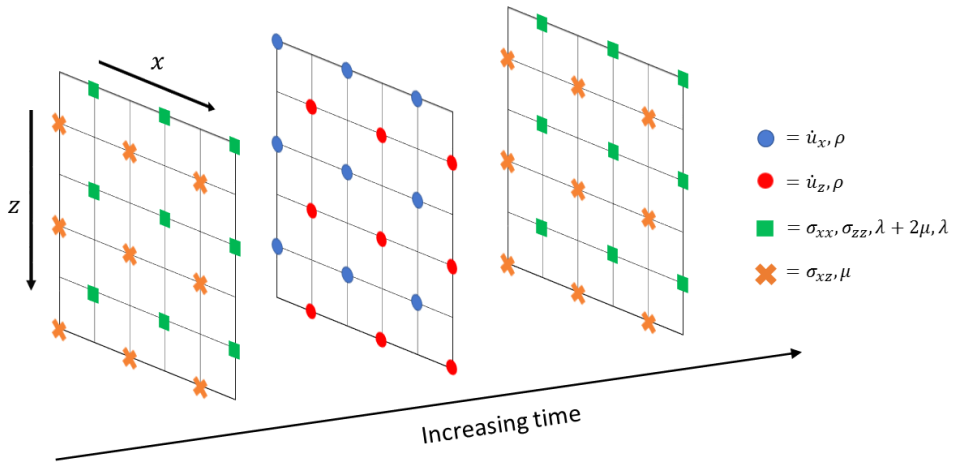


FIG. 4. Staggered grid required for solution of the 2D velocity-stress finite difference equations.

**Velocity-Stress method in three dimensions.**

Distributed Acoustic Sensing cables, and fibres are inherently three dimensional shapes, meaning in order to model their response we must model a full three dimensional wavefield. We now consider a cubic volume in which all three velocity components $\dot{u}_i$ and all six independent components of the strain tensor $\sigma_{ij}$ are, in general, nonzero. The elastodynamic equations of motion are (Yao and Margrave, 2000; Yomogida and Etgen, 1993),

$$\frac{\partial \dot{u}_x}{\partial t} = \frac{1}{\rho}\left(\frac{\partial \sigma_{xx}}{\partial x} + \frac{\partial \sigma_{xy}}{\partial y} + \frac{\partial \sigma_{xz}}{\partial z}\right) \tag{32}$$

$$\frac{\partial \dot{u}_y}{\partial t} = \frac{1}{\rho}\left(\frac{\partial \sigma_{xy}}{\partial x} + \frac{\partial \sigma_{yy}}{\partial y} + \frac{\partial \sigma_{yz}}{\partial z}\right) \tag{33}$$

$$\frac{\partial \dot{u}_z}{\partial t} = \frac{1}{\rho}\left(\frac{\partial \sigma_{xz}}{\partial x} + \frac{\partial \sigma_{yz}}{\partial y} + \frac{\partial \sigma_{zz}}{\partial z}\right) \tag{34}$$

and the time derivative stress-strain relations become,

$$\frac{\partial \sigma_{xx}}{\partial t} = (\lambda + 2\mu)\frac{\partial \dot{u}_x}{\partial x} + \lambda\left(\frac{\partial \dot{u}_y}{\partial y} + \frac{\partial \dot{u}_z}{\partial z}\right) \tag{35}$$

$$\frac{\partial \sigma_{yy}}{\partial t} = (\lambda + 2\mu)\frac{\partial \dot{u}_y}{\partial y} + \lambda\left(\frac{\partial \dot{u}_x}{\partial x} + \frac{\partial \dot{u}_z}{\partial z}\right) \tag{36}$$

$$\frac{\partial \sigma_{zz}}{\partial t} = (\lambda + 2\mu)\frac{\partial \dot{u}_z}{\partial z} + \lambda\left(\frac{\partial \dot{u}_x}{\partial x} + \frac{\partial \dot{u}_y}{\partial y}\right) \tag{37}$$

$$\frac{\partial \sigma_{xz}}{\partial t} = \mu\left(\frac{\partial \dot{u}_x}{\partial z} + \frac{\partial \dot{u}_z}{\partial x}\right) \tag{38}$$

$$\frac{\partial \sigma_{xy}}{\partial t} = \mu\left(\frac{\partial \dot{u}_x}{\partial y} + \frac{\partial \dot{u}_y}{\partial x}\right) \tag{39}$$

$$\frac{\partial \sigma_{yz}}{\partial t} = \mu\left(\frac{\partial \dot{u}_y}{\partial z} + \frac{\partial \dot{u}_z}{\partial y}\right) \tag{40}$$

where, again the isotropic stiffness tensor has been used.

*Solving the 3D velocity-stress equations.*

In the full three dimensional case the solutions to equations (32)-(40) requires keeping careful track of the indices of each value.

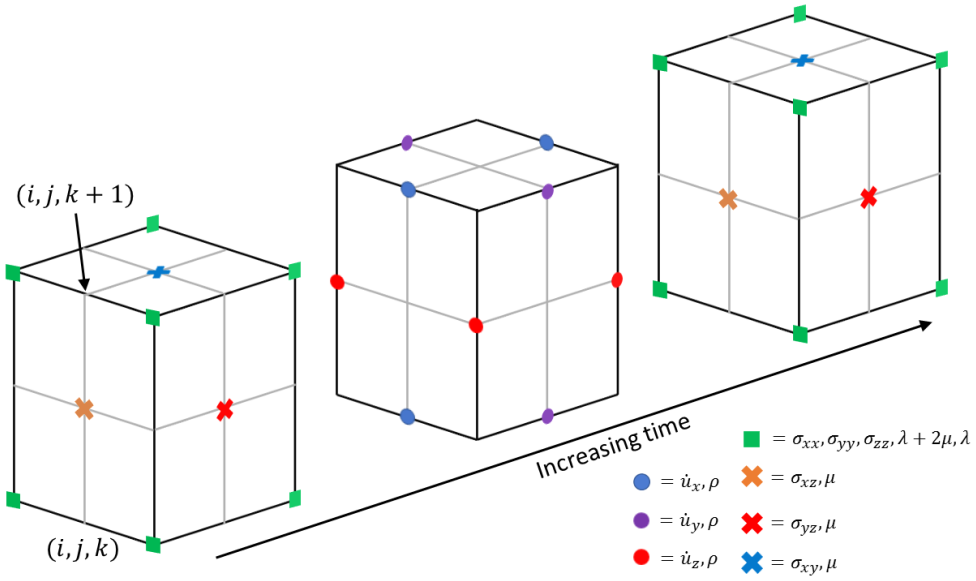


FIG. 5. Staggered grid required for solution of the 3D velocity-stress finite difference equations.

Time will be kept track of, as in the other cases with the index $n$. In figure 5 the cubic volume in the bottom left is at time level $n$, and contains values of the normal and shear stress. Normal stresses are indicated by the green squares, and shear stresses by the $x's$. Velocities are computed on a cubic grid, shifted in time by a half time step at time level

$n + 1/2$. The velocities, $\dot{u}_x$, $\dot{u}_y$, and $\dot{u}_z$ are represented by the blue, purple, and red circles respectively. Stresses are calculated at time step $n+1$ as shown on the cubic grid in the top right of figure 5.

In general, we cannot know the values of two of the velocity components at the same grid point, nor can we know the value of shear stress and normal stress at the same grid point (Virieux, 1986). Therefore we now have not only a staggered grid in time, but also staggered grids in all three spatial dimensions. If we let the velocity in the $x$-direction ($\dot{u}_x$) exist at the central node $(i, j, k)$, then each velocity and stress component has the following indexing,

$$\dot{u}_x = U^{n+\frac{1}{2}}_{i,j,k} \quad , \quad \dot{u}_y = W^{n+\frac{1}{2}}_{i+\frac{1}{2},j+\frac{1}{2},k} \quad , \quad \dot{u}_z = V^{n+\frac{1}{2}}_{i+\frac{1}{2},j,k+\frac{1}{2}}$$

$$\sigma_{xx} = \psi^{n}_{i+\frac{1}{2},j,k} \quad , \quad \sigma_{yy} = \gamma^{n}_{i+\frac{1}{2},j,k} \quad , \quad \sigma_{zz} = \Sigma^{n}_{i+\frac{1}{2},j,k}$$

$$\sigma_{xz} = \phi^{n}_{i,j,k+\frac{1}{2}} \quad , \quad \sigma_{xy} = \Pi^{n}_{i,j+\frac{1}{2},k} \quad , \quad \sigma_{yz} = \xi^{n}_{i+\frac{1}{2},j+\frac{1}{2},k+\frac{1}{2}}$$

where the conversion $\{\dot{u}_x, \dot{u}_y, \dot{u}_z, \sigma_{xx}, \sigma_{yy}, \sigma_{zz}, \sigma_{xz}, \sigma_{xy}, \sigma_{yz}\} \rightarrow \{U, W, V, \psi, \gamma, \Sigma, \phi, \Pi, \xi\}$ was used.

Using this indexing, and notation, the finite difference solutions to the system of three velocity equations is,

$$\frac{U^{n+\frac{1}{2}}_{i,j,k} - U^{n-\frac{1}{2}}_{i,j,k}}{\tau} = \frac{1}{\rho}\big[D_x\psi + D_y\Pi + D_z\phi\big]\Big|^{n}_{i,j,k} \tag{41}$$

$$\frac{W^{n+\frac{1}{2}}_{i+\frac{1}{2},j+\frac{1}{2},k} - W^{n-\frac{1}{2}}_{i+\frac{1}{2},j+\frac{1}{2},k}}{\tau} = \frac{1}{\rho}\big[D_x\Pi + D_y\gamma + D_z\xi\big]\Big|^{n}_{i+\frac{1}{2},j+\frac{1}{2},k} \tag{42}$$

$$\frac{V^{n+\frac{1}{2}}_{i+\frac{1}{2},j,k+\frac{1}{2}} - V^{n-\frac{1}{2}}_{i+\frac{1}{2},j,k+\frac{1}{2}}}{\tau} = \frac{1}{\rho}\big[D_x\phi + D_y\xi + D_z\Sigma\big]\Big|^{n}_{i+\frac{1}{2},j,k+\frac{1}{2}} \tag{43}$$

the solutions to the system of three normal stress components is,

$$\frac{\psi^{n+1}_{i+\frac{1}{2},j,k} - \psi^{n}_{i+\frac{1}{2},j,k}}{\tau} = (\lambda + 2\mu)\big[D_xU\big]\Big|^{n+\frac{1}{2}}_{i+\frac{1}{2},j,k} + \lambda\big[D_yW + D_zV\big]\Big|^{n+\frac{1}{2}}_{i+\frac{1}{2},j,k} \tag{44}$$

$$\frac{\gamma^{n+1}_{i+\frac{1}{2},j,k} - \gamma^{n}_{i+\frac{1}{2},j,k}}{\tau} = (\lambda + 2\mu)\big[D_yW\big]\Big|^{n+\frac{1}{2}}_{i+\frac{1}{2},j,k} + \lambda\big[D_xU + D_zV\big]\Big|^{n+\frac{1}{2}}_{i+\frac{1}{2},j,k} \tag{45}$$

$$\frac{\Sigma^{n+1}_{i+\frac{1}{2},j,k} - \Sigma^{n}_{i+\frac{1}{2},j,k}}{\tau} = (\lambda + 2\mu)\big[D_zV\big]\Big|^{n+\frac{1}{2}}_{i+\frac{1}{2},j,k} + \lambda\big[D_xU + D_yW\big]\Big|^{n+\frac{1}{2}}_{i+\frac{1}{2},j,k} \tag{46}$$

and finally for the shear stress components,

$$\frac{\phi^{n+1}_{i,j,k+\frac{1}{2}} - \phi^{n}_{i,j,k+\frac{1}{2}}}{\tau} = \mu\big[D_zU + D_xV\big]\Big|^{n+\frac{1}{2}}_{i,j,k+\frac{1}{2}} \tag{47}$$

$$\frac{\Pi^{n+1}_{i,j+\frac{1}{2},k} - \Pi^{n}_{i,j+\frac{1}{2},k}}{\tau} = \mu\big[D_y U + D_x W\big]\Big|^{n+\frac{1}{2}}_{i,j+\frac{1}{2},k} \tag{48}$$

$$\frac{\xi^{n+1}_{i+\frac{1}{2},j+\frac{1}{2},k+\frac{1}{2}} - \xi^{n}_{i+\frac{1}{2},j+\frac{1}{2},k+\frac{1}{2}}}{\tau} = \mu\big[D_y V + D_z W\big]\Big|^{n+\frac{1}{2}}_{i+\frac{1}{2},j+\frac{1}{2},k+\frac{1}{2}} \tag{49}$$

Equations (41)-(49) represent the 9 coupled finite difference equations that must be solved in order to propagate a three dimensional wavefield according to the velocity-stress scheme. The operators $D_i$ are spatial, central finite difference operators in the $i^{th}$ direction, centered at spatial indices to the right of the vertical bars.

These equations are solved similar to the 1D case. Assuming knowledge of all nine components everywhere on the grid at time level $n$, equations (41)-(43) are solved at time level $n+\frac{1}{2}$ at every spatial point, and then equations (44)-(49) are solved at time level $n+1$ at every spatial location. This then continues for every time step.

## COMBINING DAS GEOMETRIC MODELS AND ELASTIC WAVE PROPAGATION

We now have an elastic finite difference scheme in particle velocity and stress, and a model for a fibre that is sensitive to strain along its tangent direction. In order to tie these ideas together, we need some measure of the strain. However, it is argued that DAS is actually measuring the strain rate and not strain itself (Hornman, 2017). With this in mind, we may instead connect the two ideas by computing the strain rate. We start with the expression for a strain tensor, equation (19), and take the time derivative,

$$\frac{\partial e_{kl}}{\partial t} = \frac{1}{2}\left(\frac{\partial^2 u_k}{\partial x_l \partial t} + \frac{\partial^2 u_l}{\partial x_k \partial t}\right) = \frac{1}{2}\left(\frac{\partial \dot{u}_k}{\partial x_l} + \frac{\partial \dot{u}_l}{\partial x_k}\right) \tag{50}$$

We now have an expression for the strain rate, which conveniently relies solely on the spatial derivatives of the velocity. The velocity-stress finite difference solution has provided a volume of the velocity everywhere, at every time step, allowing us to compute volumes of the strain rate at each time step. Our strain rate tensor at each point is then,

$$\dot{e} = \frac{1}{2}\begin{bmatrix} 2\dot{u}_{x,x} & \dot{u}_{x,y} + \dot{u}_{y,x} & \dot{u}_{x,z} + \dot{u}_{z,x} \\ \dot{u}_{x,y} + \dot{u}_{y,x} & 2\dot{u}_{y,y} & \dot{u}_{y,z} + \dot{u}_{z,y} \\ \dot{u}_{x,z} + \dot{u}_{z,x} & \dot{u}_{y,z} + \dot{u}_{z,y} & 2\dot{u}_{z,z} \end{bmatrix} \tag{51}$$

Due to the stress-strain relation of equation (18), these strain rates are placed at the location of the stresses with which they correspond.

We are now left with a strain rate tensor at every point in a Cartesian grid. From our previous discussion, what we desire is a strain rate in the coordinate system of the fibre, namely $\{\hat{\mathbf{t}}(s), \hat{\mathbf{n}}(s), \hat{\mathbf{b}}(s)\}$. To rotate a tensor of rank 2, we apply the expression $\dot{e}' = R\dot{e}R^T$, where $R$ is the rotation matrix taking the strain rate from $\{\hat{\mathbf{1}}, \hat{\mathbf{2}}, \hat{\mathbf{3}}\}$ to $\{\hat{\mathbf{t}}(s), \hat{\mathbf{n}}(s), \hat{\mathbf{b}}(s)\}$.

$$\begin{bmatrix} \dot{e}_{tt} & \dot{e}_{tn} & \dot{e}_{tb} \\ \dot{e}_{nt} & \dot{e}_{nn} & \dot{e}_{nb} \\ \dot{e}_{bt} & \dot{e}_{bn} & \dot{e}_{bb} \end{bmatrix} = R \begin{bmatrix} 2\dot{u}_{x,x} & \dot{u}_{x,y} + \dot{u}_{y,x} & \dot{u}_{x,z} + \dot{u}_{z,x} \\ \dot{u}_{x,y} + \dot{u}_{y,x} & 2\dot{u}_{y,y} & \dot{u}_{y,z} + \dot{u}_{z,y} \\ \dot{u}_{x,z} + \dot{u}_{z,x} & \dot{u}_{y,z} + \dot{u}_{z,y} & 2\dot{u}_{z,z} \end{bmatrix} R^T \tag{52}$$

with

$$R = \begin{bmatrix} \hat{\mathbf{t}} \cdot \hat{\mathbf{1}}(s) & \hat{\mathbf{t}} \cdot \hat{\mathbf{2}}(s) & \hat{\mathbf{t}} \cdot \hat{\mathbf{3}}(s) \\ \hat{\mathbf{n}} \cdot \hat{\mathbf{1}}(s) & \hat{\mathbf{n}} \cdot \hat{\mathbf{2}}(s) & \hat{\mathbf{n}} \cdot \hat{\mathbf{3}}(s) \\ \hat{\mathbf{b}} \cdot \hat{\mathbf{1}}(s) & \hat{\mathbf{b}} \cdot \hat{\mathbf{2}}(s) & \hat{\mathbf{b}} \cdot \hat{\mathbf{3}}(s) \end{bmatrix} \tag{53}$$

The fibre is only sensitive to the $\dot{e}_{tt}$ component of the strain tensor in the $\{\hat{\mathbf{t}}, \hat{\mathbf{n}}, \hat{\mathbf{b}}\}$ frame. The formula for which is,

$$\dot{e}_{tt} = \dot{e}_{11}(\hat{\mathbf{t}}\cdot\hat{\mathbf{1}})^2 + 2\dot{e}_{12}(\hat{\mathbf{t}}\cdot\hat{\mathbf{1}})(\hat{\mathbf{t}}\cdot\hat{\mathbf{2}}) + 2\dot{e}_{13}(\hat{\mathbf{t}}\cdot\hat{\mathbf{1}})(\hat{\mathbf{t}}\cdot\hat{\mathbf{3}}) + \dot{e}_{22}(\hat{\mathbf{t}}\cdot\hat{\mathbf{2}})^2 + 2\dot{e}_{23}(\hat{\mathbf{t}}\cdot\hat{\mathbf{2}})(\hat{\mathbf{t}}\cdot\hat{\mathbf{3}}) + \dot{e}_{33}(\hat{\mathbf{t}}\cdot\hat{\mathbf{3}})^2 \tag{54}$$

Applying equation (54) for each point along the fibre, at each time step, will provide the DAS fibre seismogram for an arbitrary cable and fibre geometry.

## EXAMPLES

To test the efficacy of our coupled DAS shaped-fibre and 3D elastic finite difference wave model we will utilize a simple homogeneous model that is 500x500x500 meters, with a point source located at the position (250,250,250) meters. We will look at the response of simulated 1-C geophones to the vertical component of velocity, both to compare the complexities in computing a geophone response versus a DAS fibre response, and to examine the broadside insensitivity of DAS fibres. Additionally, we will also look at the response of straight, helically wound, and nested two-helix DAS fibres.

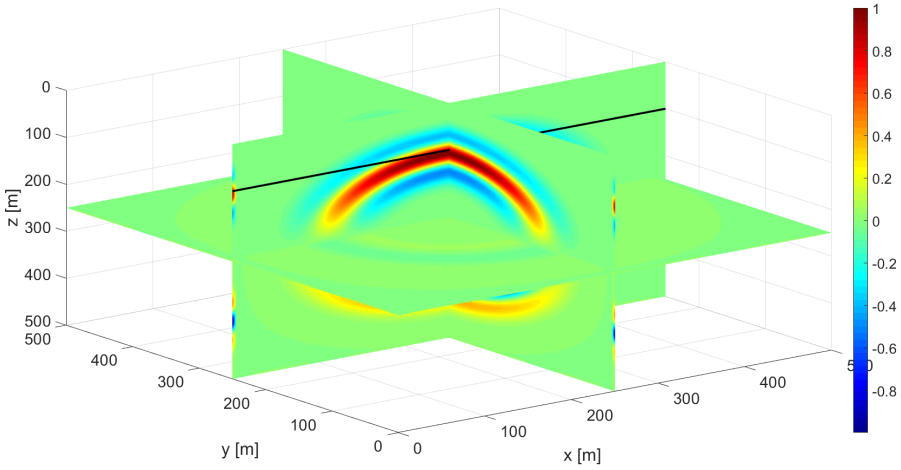


FIG. 6. Snap shot of the vertical component of velocity, black line represents a line of 1-C vertical geophones.

Figure 6 shows a snapshot of the vertical component of particle velocity as the wavefield propagates through the line of 1-C geophones in the $x - z$ plane shown by the black line. Taking the values of this snapshot at the location of the geophones provides the response of the 1-C geophones at the time of the snapshot. Doing this for all snapshots of the wavefield produces the conventional shot record we are used to dealing with, shown in figure 7. While this example is straightforward, it emphasizes the fact that the wavefield recorded by 1-C geophones is relatively simple.

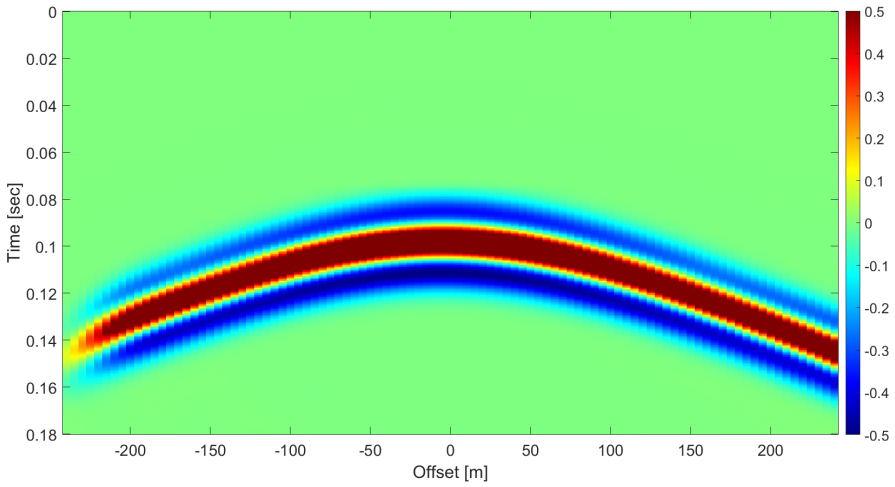


FIG. 7. Shot record of vertical velocity.

Figure 8 shows snapshots of the six independent components of strain required to compute the response of the fibre. The normal strains are shown in the top row with $e_{xx}$ in (a), $e_{yy}$ in (b), and $e_{zz}$ in (c). The shear components of strain are displayed in the bottom row with $e_{xy}$ in (d), $e_{xz}$ in (e), and $e_{yz}$ in (f). The black line in figure 8 represents the central axis of either a straight, helical, or nested two-helix fibre. To compute the response of the DAS fibre at a given time these six strain components must be rotated onto the fibre, and then summed according to equation (50). Repeating this for all times steps produces the shot record that would be recorded with a DAS fibre. Figure 8 emphasizes the fact that the wavefield a DAS fibre is measuring is much more complex than the wavefield being measured by a standard geophone.

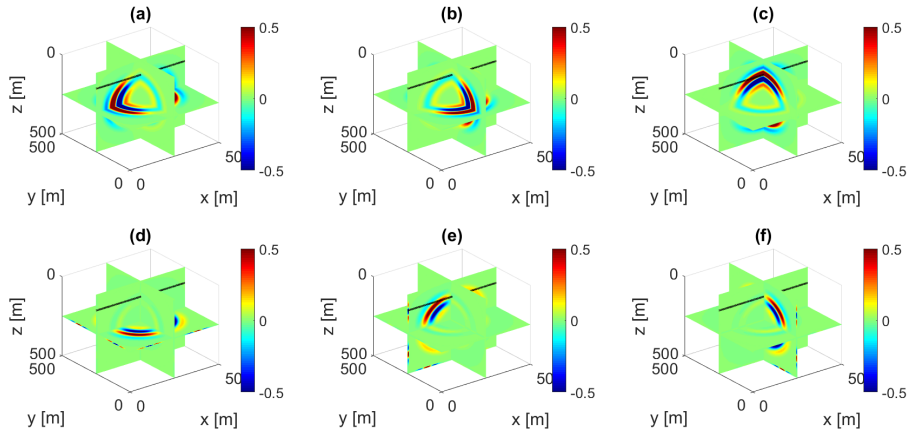


FIG. 8. Snap shot of stain components, the black line indicates the central axis of the straight, one helix, or two helix fibre. (a) strain component $e_{xx}$, (b) strain component $e_{yy}$, (c) strain component $e_{zz}$, (d) strain component $e_{xy}$, (e) strain component $e_{xz}$, (f) strain component $e_{yz}$.

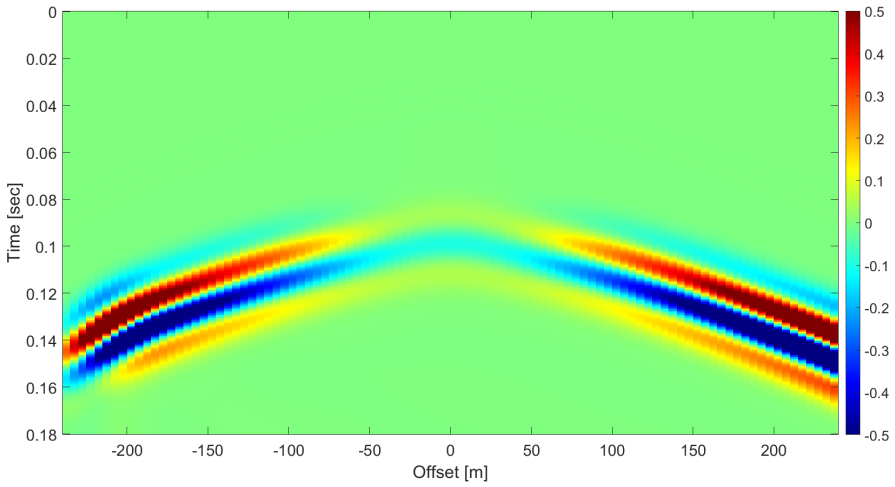


FIG. 9. Response of straight DAS fibre to a varying wavefield.

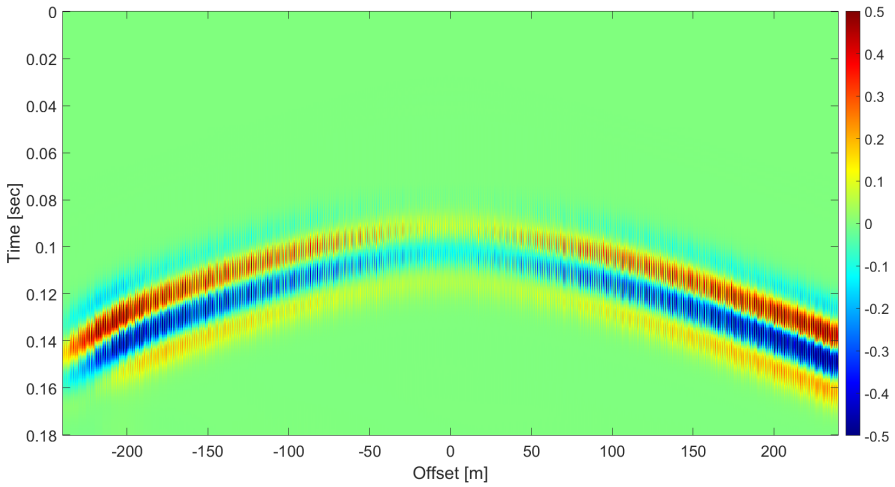


FIG. 10. Response of a helically wound DAS fibre to a varying wavefield.

Figure 9 shows the response of a straight fibre in the $x - z$ plane, while figures 10 and 11 show the responses of a one-helix, and two-helix fibre respectively. Comparing figure 9 to figure 7 shows the well known broadside insensitivity of DAS fibres to impinging wavefields. Kuvshinov (2015) showed that the amplitude of DAS fibre measurements has $\cos^2(\theta)$ dependence, where $\theta$ is the angle between the inbound wavefield and the tangent of the fibre. Therefore, for normally incident wavefield we expect the response to be zero, and amplitudes to be weak at near offsets as shown in figure 9. Naturally, if we construct a fibre with a varying tangent, then a wavefield that was previously normally incident on a straight fibre will only be normally incident on some sections of the new fibre. As a helical wound fibre rotates around its principal axis portions of the fibre will be non-normally incident with the wavefield and we should reduce the broadside insensitivity by sampling more tangents. Figure 10 shows that when a one-helix fibre is used, we can better recover the amplitudes in the central portion of the hyperbola. As we sample more tangent directions with more complicated geometries such as the two-helix, we recover even more of the wavefield, as shown in figure 11. In figure 11 we see a somewhat stripy appearance in

the recovered wavefield, which results from the helix wind. A nested two-helix has a winding cable, and a fibre winding around that cable, and as such the fibre-cable system has two periods of rotation. The striped appearance of the wavefield is a results of these two periods. The small scale stripped appearance, similar to the one-helix case is caused by the tight winding of the fibre, while the large period stripped appearance is cause by the larger period wind of the cable. As the cable and fibre winds, the fibre tangent alternately becomes inline, and perpendicular to the wavefield, the result being that the amplitudes vary with the wind, which is causing the stripped appearance. This creates gaps in the signal when the fibre becomes perpendicular to the wavefield, but has the advantage of allowing us to recover signal in the center of the shot, and overall reduces the broadside insensitivity.

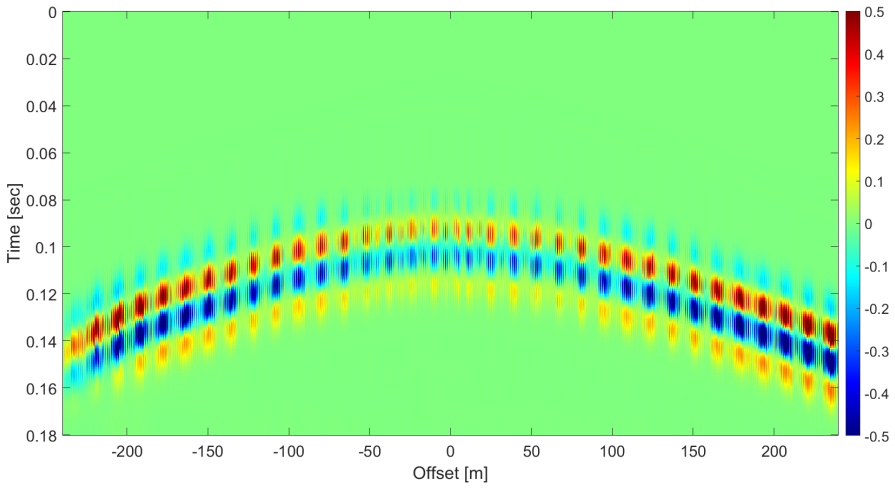


FIG. 11. Response of a nested two-helix DAS fibre to a varying wavefield.

## CONCLUSIONS

We set out with the goal of coupling a geometrical model of an arbitrarily shaped DAS fibre and a 3D elastic wave model, so that we could model the response of a DAS fibre to a propagating wavefield. We began with a discussion of the cable and fibre geometries, and discussed the computation of the important tenants of each. Specific focus was given to the fibre tangent directions which must be carefully kept track of in order to know which portion of the wavefield a fibre is sampling. We then discussed the velocity-stress method of finite difference modeling in both 1 and 3 dimensions. It was then shown that the velocity-stress method can be utilized to compute the strain rate tensor at each grid location for a given time step. Rotation of the strain rate tensor onto the fibre tangents at each time step then provides the response of the DAS fibre. We then showed examples of the response of a straight fibre, helically wound fibre, and nested two-helix fibre to a propagating wavefield generated by a point source. In the straight fibre case we saw the well known broadside insensitivity confirming our approach provides accurate results. The one-helix, and two-helix fibres were shown to reduce the effect of broadside insensitivity on the recorded wavefield. The successful coupling of a geometrical model of an arbitrarily shaped DAS fibre and a 3D elastic wave model opens the door to test processing schemes, wavefield suppression, and further research into the application of DAS fibres.

## ACKNOWLEDGMENTS

The authors would like to thank the sponsors of the CREWES project as well NSERC under the grant CRDPJ 461179-13 for making this work possible through their financial support.

## REFERENCES

Daley, T., Freifeld, B., Ajo-Franklin, J., Dou, S., Pevzner, R., Shulakova, V., Kashikar, S., Miller, D., Goetz, J., Henninges, J., and Lueth, S., 2013, Field testing of fibre-optic Distributed Acoustic Sensing (DAS) for subsurface seismic monitoring.: The Leading Edge.

Hornman, J., 2017, Field trial of seismic recording using Distributed Acoustic Sensing with broadside sensitive fibre-optic cables.: Geophysical Prospecting, **65**, No. 1.

Innanen, K., 2017, Determination of seismic-tensor strain from helical wound cable-Distributed Acoustic Sensing cable with arbitrary and nested-helix winds.: SEG Expanded Abstracts.

Krebes, S., 2010, Geophysics 665: Course Notes:

Kuvshinov, B., 2015, Interaction of helically wound fibre-optic cables with plane seismic waves.: Geophysical Prospecting, **65**, No. 3, 671–688.

Martin, E., Biondi, B., Cole, S., and Karrenbach, M., 2017, Continuous subsurface monitoring by passive seismic data recorded with Distributed Acoustic Sensors: the "Stanford DAS Array" experiment.: EAGE Expanded Abstracts.

Mateeva, A., Lopez, J., Potters, H., Mestayer, J., Cox, B., Kiyashchenko, D., Wills, P., Grandi, S., Hornman, K., Kuvshinov, B., Berlang, W., Yang, Z., and Detomo, R., 2014, Distributed Acoustic Sensing for reservoir monitoring with vertical seismic profiling.: Geophysical Prospecting, **62**.

Mestayer, J., Karam, S., Cox, B., Wills, P., Mateeva, A., Lopez, J., Hill, D., and Lewis, A., 2012, Distributed Acoustic Sensing for geophysical monitoring.: EAGE Expanded Abstracts.

Pressley, A., 2010, Elementary Differential Geometry: Springer, 2nd edn.

Virieux, J., 1986, P-SV wave propagation in heterogeneous media: velocity-stress finite difference method.: Geophysics, **51**, No. 4.

Webster, P., Molenaar, M., and Perkins, C., 2016, DAS microseismic: CSEG Recorder Focus Article, 38–39.

Yao, Z., and Margrave, G., 2000, Elastic wavefield modeling in 3D by fourth-order staggered-grid finite difference techniques: CREWES Research Report, **12**, No. 11.

Yomogida, K., and Etgen, J., 1993, 3-D wave propagation in the Los Angeles basin for the Whittier-Narrows earthquake: Bulletin of the Seismological Society of America, **83**, No. 5.

## APPENDIX A: SECOND ORDER AND FOURTH ORDER FINITE DIFFERENCE OPERATORS

In equations (41)-(49) it was indicated the symbol $D_\alpha$ was a centered finite difference in the direction governed by $\alpha$, centered at the indices on the right of the vertical bar. For instance in equation (41) the term $D_x$ is a CFDA, in the $x$-direction, centered at $i, j, k$. One approximation to this CFDA, in the $x$-direction is,

$$D\psi_m = \frac{\psi_{m+\frac{1}{2}} - \psi_{m-\frac{1}{2}}}{h} \tag{55}$$

We will now examine the truncation error by expanding each term in a Taylor series,

$$\begin{aligned} hD\psi_m &= \left(\psi_m + \psi'_m \frac{h}{2} + \frac{1}{2}\psi''_m \left(\frac{h}{2}\right)^2 + \frac{1}{6}\psi'''_m \left(\frac{h}{2}\right)^3 + ...\right) \\ &-\left(\psi_m - \psi'_m \frac{h}{2} + \frac{1}{2}\psi''_m \left(\frac{h}{2}\right)^2 - \frac{1}{6}\psi'''_m \left(\frac{h}{2}\right)^3 + ...\right) \\ &= h\psi'_m + \frac{1}{24}\psi''_m h^3 + ... \end{aligned}$$

and therefore,

$$D\psi_m = \psi'_m + \frac{1}{24}\psi''_m h^2 + ...$$

showing that equation (55) has truncation error of $O(h^2)$, and is commonly termed the second order approximation.

It can be shown that the next highest order approximation has the form,

$$D\psi_m = \frac{-\psi_{m+\frac{3}{2}} + 27\psi_{m+\frac{1}{2}} - 27\psi_{m-\frac{1}{2}} + \psi_{m-\frac{3}{2}}}{24h} \tag{56}$$

Again expanding each term by its Taylor series,

$$\begin{aligned} hD\psi_m = &\frac{-1}{24}\left(\psi_m + \psi'_m \frac{3}{2}h + \frac{1}{2}\psi''_m \left(\frac{3}{2}h\right)^2 + \frac{1}{6}\psi'''_m \left(\frac{3}{2}h\right)^3 + \frac{1}{24}\psi^{(4)}_m \left(\frac{3}{2}h\right)^4 + \frac{1}{120}\psi^{(5)}_m \left(\frac{3}{2}h\right)^5 + ...\right) \\ &+\frac{27}{24}\left(\psi_m + \psi'_m \frac{1}{2}h + \frac{1}{2}\psi''_m \left(\frac{1}{2}h\right)^2 + \frac{1}{6}\psi'''_m \left(\frac{1}{2}h\right)^3 + \frac{1}{24}\psi^{(4)}_m \left(\frac{1}{2}h\right)^4 + \frac{1}{120}\psi^{(5)}_m \left(\frac{1}{2}h\right)^5 + ...\right) \\ &-\frac{27}{24}\left(\psi_m - \psi'_m \frac{1}{2}h + \frac{1}{2}\psi''_m \left(\frac{1}{2}h\right)^2 - \frac{1}{6}\psi'''_m \left(\frac{1}{2}h\right)^3 + \frac{1}{24}\psi^{(4)}_m \left(\frac{1}{2}h\right)^4 - \frac{1}{120}\psi^{(5)}_m \left(\frac{1}{2}h\right)^5 + ...\right) \\ &\frac{1}{24}\left(\psi_m - \psi'_m \frac{3}{2}h + \frac{1}{2}\psi''_m \left(\frac{3}{2}h\right)^2 - \frac{1}{6}\psi'''_m \left(\frac{3}{2}h\right)^3 + \frac{1}{24}\psi^{(4)}_m \left(\frac{3}{2}h\right)^4 - \frac{1}{120}\psi^{(5)}_m \left(\frac{3}{2}h\right)^5 + ...\right) \end{aligned}$$

resulting in,

$$D\psi_m = \psi_m - \frac{3}{640}\psi^{(5)}_m h^4 + ...$$

showing that equation (56) has truncation error $O(h^4)$ and is commonly referred to as the fourth order approximation. When greater numerical accuracy is desired, the fourth order approximation is used, and when efficiency is desired the second order approximation my be used.